Weighted Level Set Evolution Based on Local Edge Features for Medical Image Segmentation

Alaa Khadidos, Victor Sanchez, *Member, IEEE*, and Chang-Tsun Li, *Senior Member, IEEE*

Abstract—Level set methods have been widely used to implement active contours for image segmentation applications due to their good boundary detection accuracy. In the context of medical image segmentation, weak edges and inhomogeneities remain important issues that may hinder the accuracy of any segmentation method based on active contours implemented using level set methods. This paper proposes a method based on active contours implemented using level set methods for segmentation of such medical images. The proposed method uses a level set evolution that is based on the minimization of an objective energy functional whose energy terms are weighted according to their relative importance in detecting boundaries. This relative importance is computed based on local edge features collected from the adjacent region located inside and outside of the evolving contour. The local edge features employed are the edge intensity and the degree of alignment between the image's gradient vector flow field and the evolving contour's normal. We evaluate the proposed method for segmentation of various regions in real MRI and CT slices, X-ray images, and ultra sound images. Evaluation results confirm the advantage of weighting energy forces using local edge features to reduce leakage. These results also show that the proposed method leads to more accurate boundary detection results than state-of-the-art edge-based level set segmentation methods, particularly around weak edges.

Index Terms—image segmentation, medical images, active contours, level set methods.

I. INTRODUCTION

Image segmentation is an important analysis tool in many applications of computer vision, machine learning and image analysis [1]–[13]. In medical imaging, segmentation helps extracting local information from the imaging data that can aid in clinical and diagnosis procedures [14]–[21]. State-of-the-art segmentation techniques are usually formulated as an optimization problem, where the segmentation criteria and the contour characteristics are specified by an objective functional.

Osher *et al.* [22] propose the level set method which implicitly represents a curve as the zero level of the level set, ϕ, of a high dimensional function. Level set methods have been successfully used to implement active contours for segmentation applications. The basic idea is to represent contours as the level set function and to evolve the level set function according to a partial differential equation (PDE) [2], [23], [24]. This approach allows to automatically handle

Alaa Khadidos is with the Department of Computer Science, University of Warwick, Coventry CV4 7AL, UK. He is also with the Faculty of Computing and Information Technology,King Abdulaziz University, Jeddah, Saudi Arabia (e-mail: a.khadidos@warwick.ac.uk; khadidos@kau.edu.sa).

Victor Sanchez is with the Department of Computer Science, University of Warwick, Coventry CV4 7AL, UK, (e-mail: vsanchez@dcs.warwick.ac.uk).

Chang-Tsun Li is with School of Computing and Mathematics, Charles Sturt University, Australia, (e-mail: chli@csu.edu.au).

the topological changes of the boundary to be detected [25]. The evolution PDE of the level set function can be directly derived from the problem of minimizing a certain energy functional defined on the level set function. This type of variational methods, which are known as variational level set methods, are highly amenable to incorporating additional information in the level set evolution (LSE), such as region-based information [2], [6], shape-prior information [26] and phase-based information [19], which usually gives rise to very accurate boundary detection results.

Recently, several authors have proposed segmentation approaches that employ variational level set methods that incorporate different image features into the energy functional. These methods, which have also been used to develop medical image segmentation approaches, aim at solving common issues that hinder segmentation accuracy, such as leakage around weak edges and high sensitivity to intensity inhomogeneities [19], [27]–[35], [35]–[42]. For example, Kimmel [29] propose an active contour that employs a level set method with an energy functional that combines an alignment term that leads the curve to the boundary of the desired region. Specifically, the alignment term attempts to align the normal vector of the zero level set with the image's gradient. Although this alignment term leads to more accurate segmentation results, the method may fail to accurately drive the zero level set to the desired boundary around weak edges due to the fact that the gradient of the image around weak edges is relatively small [31]. Belaid *et al.* [19] propose a phase-based level set (PBLS) method to implement an active contour for segmentation of medical images with high levels of noise and weak edges. In their approach, the authors construct a speed term based on two phase features: local phase, which is derived from the monogenic signal; and local orientation, which measures the alignment between the local image orientations and the contour's normal direction of movement. PBLS has shown to perform very well in the presence of weak edges, despite requiring a careful tuning of the parameters associated with the edge map used by the method [43]. Estellers *et al.* [31] propose a segmentation method based on the geometric representation of images as 2D manifolds embedded in a higher dimensional space. Their method, termed harmonic active contours (HAC), aligns the image's gradient with the gradient of the level set function for all the level sets. This results in an objective functional that is able to exploit the alignment of the neighboring level sets to pull the contour to the right position. Although HAC has been shown to provide excellent segmentation results on medical images, it may perform poorly on images with several intensity inhomogeneities [44]. Zhou

et al. [21] propose to combine an edge-based active contour model and region-based active contour model for segmentation of the left ventricle in cardiac CT images. Based on the image gradient, their method adjusts the effect of the two models. Although this method shows good performance around weak edges, the results are highly dependant on the placement of the initial contour. Ji *et al.* [20] propose a local region-based active contour model for medical image segmentation that uses the spatially varying mean and variance of local intensities to construct a local likelihood image fitting (LLIF) energy functional. Their method performs well in images with low contrast and intensity inhomogeneities. However, as with other region-based active contour models, it assumes the existence of two well-differentiated regions, which may not always be true in medical images.

Motivated by our previous work [45], we propose a segmentation method that employs an active contour implemented using a variational level set method that weights the level set evolution according to local edge features in order to accurately drive the motion of the zero level set towards the desired boundary. Specifically, our method controls the influence of energy terms in the objective functional with a weighting function that takes into account two local edge features: edge intensities and edge orientations. We employ the gradient vector flow (GVF) field of the image [46] as a measurement of local edge orientations.

Although previously proposed methods also employ local features to control the contour's evolution [8], [21], [47], [48], they usually achieve this by incorporating additional energy terms and employing a set of empirically selected parameters to specify the influence of these terms. This may lead to inaccurate segmentation results, especially around weak edges. Other methods not based on level set methods employ edge information to balance the linear combination of energy terms in graph cut segmentation, as in [49]. In this work, instead of incorporating additional energy terms, our method employs a weighting approach to determine the effect of the two basic energy terms usually employed in edge-based active contours implemented using level-set methods: the *area* and *length* terms. Specifically, the novelties of our approach are as follows:

1) Our method measures the alignment between the evolving contour's normal direction of movement and the image's gradient in the adjacent region located inside and outside of the evolving contour. Other methods that also measure this alignment, e.g., [29], [31], usually do this only in the adjacent region of the evolving contour in the direction of movement. Moreover, this measurement is often used as an additional energy term in the energy functional.

2) Our method also considers the average edge intensity in the adjacent region located inside and outside of the evolving contour. This allows to minimize the negative effect of weak edges on the segmentation accuracy.

3) Our method uses all of the collected local edge information to compute a single value that serves as a weight to control the influence of forces associated with two basic energy terms: the *area* and *length* terms. This minimizes

leakage in areas where weak edges exist.

We test the performance of the proposed method on a great variety of challenging medical images from MRI and CT sequences featuring weak edges and intensity inhomogeneities, as well as X-ray and ultra sound images. We compare our method's performance to that of state-of-the-art edge-based level-set approaches, specifically, reinitialization-free level set evolution via reaction diffusion (RD) [32], active contours based on gradient vector interaction and constrained level set diffusion (LSD) [8], distance regularized level set evolution (DRLSE) [13]. We also compare our method to PBLS [19] and Kimmel's method [29]. Results show that our proposed method attains a high boundary detection accuracy, particularly in areas prone to leakage.

The rest of the paper is organized as follows. Section II details our proposed method. Extensive experimental results for segmentation of real medical images are presented Section III. Section IV concludes this paper.

II. WEIGHTED LEVEL SET EVOLUTION

For medical image segmentation applications based on active contours implemented using variational level set methods, a variety of image information, such as intensity, edge or texture, can be used to define an objective functional. Here, we employ edge information as the main image feature that drives the evolving contour to the desired boundary. We use the following edge indicator function to acquire information about the intensities of edges:

$$g \triangleq \frac{1}{1 + |\nabla G_\sigma * I|^2} \tag{1}$$

where $g \in [0, 1]$, I is an image on a domain Ω, G_σ is a Gaussian kernel with a standard deviation σ, and $*$ denotes a convolution operation. Function g usually takes smaller values at object boundaries than at smooth regions. Based on g, we define the following basic energy functional for an Level Set Function (LSF), ϕ:

$$\mathcal{E}(\phi) = \mathcal{R}(\phi) + Length(\phi) + Area(\phi) \tag{2}$$

where $\mathcal{R}(\phi)$ is a distance regularization term as introduced in [13], and $Length(\phi)$ and $Area(\phi)$ are the length and area energy terms, respectively. Term $\mathcal{R}(\phi)$ is employed to maintain a desired shape of the LSF, as it has been previously shown that the LSF usually becomes too flat or too steep near the zero level set, resulting in numerical errors which may eventually affect the stability of the evolution [13], [32], [50], [51]. Term $Length(\phi)$ is related to the energy along the length of the evolving contour C, i.e., for the case where $\phi = 0$; while term $Area(\phi)$ is related to the energy of the area inside of C, i.e., for the case where $\phi >= 0$. These two energy terms can be defined so that the overall energy is minimized at the desired boundaries according to the edge indicator in Eq. (1):

$$Length\{\phi = 0\} = \int_\Omega g\delta(\phi) |\nabla \phi| \, d\mathbf{x} \tag{3}$$

and

$$Area\{\phi \geq 0\} = \int_{\Omega} gH(\phi)d\mathbf{x} \tag{4}$$

where H is the Heaviside function. Note that according to Eq. (3)-(4), the minimization of the these two energy terms depends heavily on the amount of edge information in the image. The Dirac delta function δ in Eq. (3) is used to compute a line integral of the edge indicator function g along the zero level set of ϕ. The Heaviside function in Eq. (4), on the other hand, is used to compute the energy of the area inside the evolving contour, C. $Length(\phi)$ is then minimized when the zero level set of ϕ is located at the object's boundary, while $Area(\phi)$ serves as a way to control the evolution speed of the zero level set. In smooth regions, $Area(\phi)$ speeds up the evolution. In regions with a high number of edges, $Area(\phi)$ slows down the evolution, which helps the contour to conform to the desired boundary. For cases in which the image comprises smooth regions delimited by strong edges, the minimization of the energy functional in Eq. (2) provides excellent boundary detection results. However, for cases where the image comprises regions with intensity inhomogeneities or delimited by weak edges, such as in medical images, the evolution process may result in an inaccurate boundary detection or leakages. In this work, we are interested in improving the accuracy of the evolution process in conforming to the desired boundaries in cases where edges are weak, and regions contain intensity inhomogeneities. To this end, we propose a weighting function to assign different priorities to the area and length terms according to the image features of the adjacent region located inside and outside of C. These features are the average edge intensity, denoted by $\mathcal{I}$, and average difference between the direction of the image's GVF and the normal direction of movement of C, denoted by γ. Note that analyzing the adjacent region located both inside and outside of C, provides an accurate insight of the location of edges, which helps the zero level set to accurately conform to the desired boundary [45].

Our proposed length and area terms then include a weighting factor, ω, that determines their importance in locating the desired boundary according to local edge features. These terms are defined as:

$$Length_2\{\phi = 0\} = \int_{\Omega} g(1 - \omega(\phi, k))\delta(\phi)\left|\nabla\phi\right|d\mathbf{x} \tag{5}$$

and

$$Area_2\{\phi \geq 0\} = \int_{\Omega} g\omega(\phi, k)H(\phi)d\mathbf{x} \tag{6}$$

where k is a constant that determines the size of the region adjacent to C from where local edge features are obtained. Weight $\omega(\phi, k)$ is given by:

$$\omega(\phi, k) = \mathcal{I}(\phi, k)^{(1 - \gamma(\phi, k))} \tag{7}$$

where $\mathcal{I} \in [0, 1]$ is the average intensity of the edge indicator along $2k$ contours adjacent to C; $\gamma \in [-1, 1]$ is the inner product between the normal of C, denoted by $\vec{N} = \nabla\phi/\left|\nabla\phi\right|$, and the GVF field along $2k$ contours adjacent to C. A contour

adjacent to C is defined as follows:

$$\psi(\phi, m) = \delta(\phi)\left|\nabla\phi\right| + m\vec{N} \tag{8}$$

where $m \in \mathbb{Z}$ and its sign denotes if the adjacent contour is located outside $(+)$ or inside $(-)$ of C. Note that with the Dirac delta function, the term $m\vec{N}$ in Eq. (8) results in a contour displaced from the zero level set of ϕ by m units in its normal direction. This is illustrated in Fig. 1.
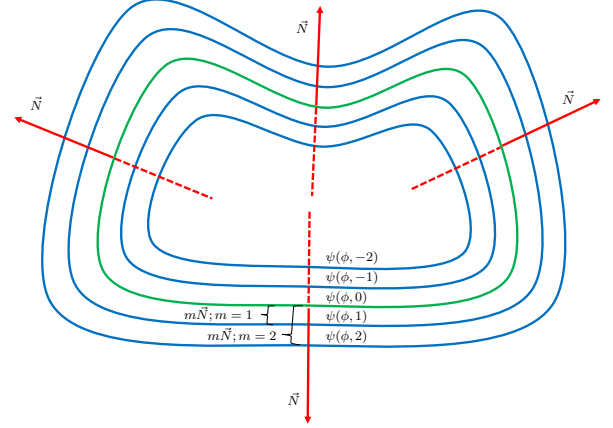

Fig. 1. The green line represents the evolving contour C, i.e., the zero level set $\psi(\phi, 0)$. The blue lines represent the adjacent contours for $m = 1$, $m = -1$, $m = 2$ and $m = -2$, as specified in Eq. (8)

The average intensity of the edge indicator along the $2k$ adjacent contours is calculated as follows:

$$\mathcal{I}(\phi, k) = \frac{1}{2k}\sum_{m=1}^{k}\left[\int_{\Omega}(1 - g)\psi(\phi, m)d\mathbf{x}\right.$$
$$\left. + \int_{\Omega}(1 - g)\psi(\phi, -m)d\mathbf{x}\right] \tag{9}$$

Similarly to the length term in Eq. (3), the integral in Eq. (9) computes the line integral of the function $(1-g)$ along two contours adjacent to C; the first one located k units from C in its outside region, and the second one located k units from C in its inside region. Note that in Eq. (9), we use the inverse value of the edge indicator g, i.e., $(1-g)$, as we are interested in determining if the $2k$ adjacent contours are located in areas with strong edge information.

We observe that the direction of the image's GVF field is a good estimator of the orientation and direction of edges [29]. Based on this observation, we calculate the alignment between the normal vector of C and the GVF field along the $2k$ adjacent contours, as illustrated in Fig. 2. The average inner product γ is then calculated as follows:

$$\gamma(\phi, k) = \frac{1}{2k}\sum_{m=1}^{k}\left[\int_{\Omega}\left\langle\vec{N}, \vec{V}\right\rangle\psi(\phi, m)d\mathbf{x}\right.$$
$$\left. + \int_{\Omega}\left\langle\vec{N}, \vec{V}\right\rangle\psi(\phi, -m)d\mathbf{x}\right] \tag{10}$$

where $\vec{V}$ denotes the image's GVF field. In this case, the integral in Eq. (10) computes the line integral of the inner product between $\vec{N}$ and $\vec{V}$ along the contours adjacent to C. Note that γ results in values close to 1 when the normal vector of C aligns with $\vec{V}$.
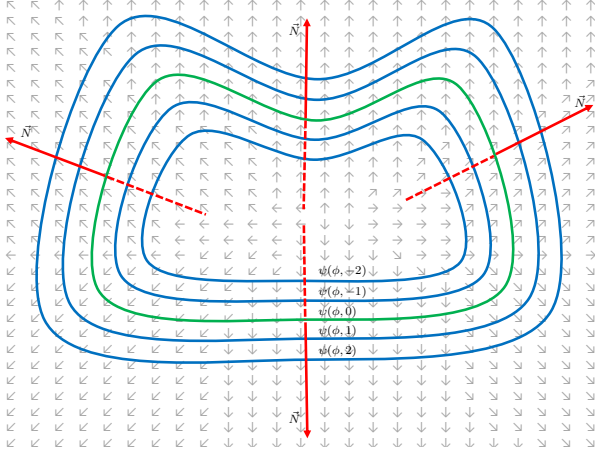

Fig. 2. The red arrow represents the normal direction of movement of the evolving contour C. Gray arrows represent the GVF field vectors, $\vec{V}$. The figure shows the case of $k = 2$.

By replacing $Length(\phi)$ and $Area(\phi)$ in Eq. (2) with $Length_2(\phi)$ and $Area_2(\phi)$ as formulated in Eq. (5) and (6), respectively, our proposed energy functional is then defined as:

$$\mathcal{E}(\phi) = \mu \int_\Omega p(|\nabla\phi|)d\mathbf{x} + (1 - \omega(\phi, k)) \int_\Omega g\delta(\phi) |\nabla\phi| \, d\mathbf{x}$$
$$+ (\omega(\phi, k)) \int_\Omega gH(\phi)d\mathbf{x}$$
(11)

where $\mu > 0$ is a constant, and $p(s) \triangleq \frac{1}{2}(s-1)^2$ is a potential (or energy density) function with a minimum point $s = 1$ that minimizes the distance regularization term $\mathcal{R}$ when $|\nabla\phi| = 1$ [13]. The energy functional in Eq. (11) can then be minimized by solving a gradient flow as follows:

$$\frac{\partial\phi}{\partial t} = \mu \mathbf{div}(d_p(|\nabla\phi|)\nabla\phi)$$
$$+ (1 - \omega(\phi, k))\delta(\phi)\mathbf{div}(g\frac{\nabla\phi}{|\nabla\phi|}) + \omega(\phi, k)g\delta(\phi)$$
(12)

where d_p is a function defined using the first derivative of $p(s)$ as $d_p(s) \triangleq \frac{p'(s)}{s}$ [13]. It is important to mention that in Eq. (12), the weighting term $\omega(\phi, k)$, although expressed as a function of ϕ and k, results in a constant value in the range $[0, 1]$. Consequently, it is regarded as a constant when computing the partial derivative with respect to time t. The weighting function $\omega(\phi, k)$ assigns different priorities to the length and area terms according to local edge features. These features are the edge intensity, $\mathcal{I}$, and the degree of alignment, γ, between $\vec{V}$ and C's normal direction of movement. Fig. 3 shows the plot of $\omega(\phi, k)$ for various values of $\mathcal{I}$ and γ. It can be seen that ω approaches 0 for large $\mathcal{I}$ values regardless of

the value of γ, i.e., when the zero level set is located in a non-smooth region. In this case, the $Length_2$ term acts as the main
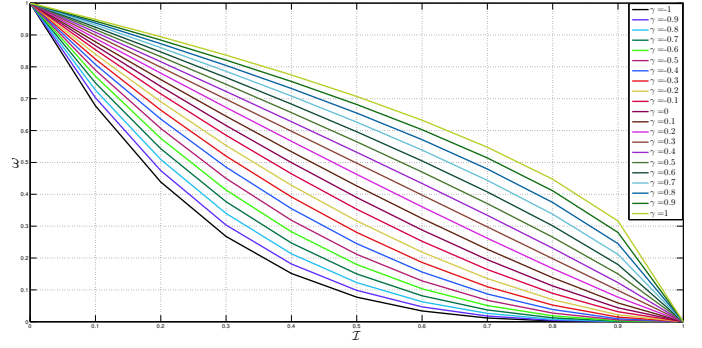

Fig. 3. Value of ω for different values of $\mathcal{I}$ and γ.

energy driving the zero level set to the object's boundary. It can also be seen that ω approaches 1 for small $\mathcal{I}$ values regardless of the value of γ. In this case, the $Area_2$ term acts as the main energy driving the zero level set towards the object's boundary within a smooth region. For values of γ close to 1, the value of ω slowly decreases as $\mathcal{I}$ increases. In this case, the normal direction of movement of C aligns with the direction of the image's GVF field, therefore the $Area_2$ term acts as the main energy term. For values of γ close to -1, the value of ω slowly decreases as $\mathcal{I}$ increases. In this case, the normal direction of movement of C is opposite to the direction of the image's GVF field, therefore the $Length_2$ term acts as the main energy term helping C to conform to the object's boundary.

Weight ω allows C to deform in relatively smooth areas even if its normal direction of movement is opposite to the GVF field surrounding C. This is particularly useful to initialize the contour far from the desired boundary, even in regions with intensity inhomogeneities. Fig. 4(a)-(b) illustrate this case, where ω approaches 1. Weight ω also minimizes leakages around weak edges by determining the influence of the energy terms in the evolution process according to the average intensities of edge information and the average direction of the GVF field in the inside and outside regions adjacent to C. This is illustrated in Fig. 4(c), where the value of ω slowly approaches 0. Finally, weight ω allows C to conform to the desired boundary by assigning a larger weight to the $Length_2$ term where strong edges are encountered in the inside and outside regions adjacent to C. This is illustrated in Fig. 4(d), where the value of ω approaches 1.

III. EXPERIMENTAL RESULTS

In this section, we apply our proposed method to segment different regions on various types of real medical images, including a number of synthetic images. The proposed method is compared to state-of-the-art edge-based level-set approaches, specifically RD, LSD, and DRLSE. The proposed method is also compared to PBLS, which is proposed for segmentation applications of very noisy images, such as ultra sound images. Finally, we also compare our method to Kimmel's method [29], since this method, despite of being region-based, shares many similarities with our method. It is important to note that
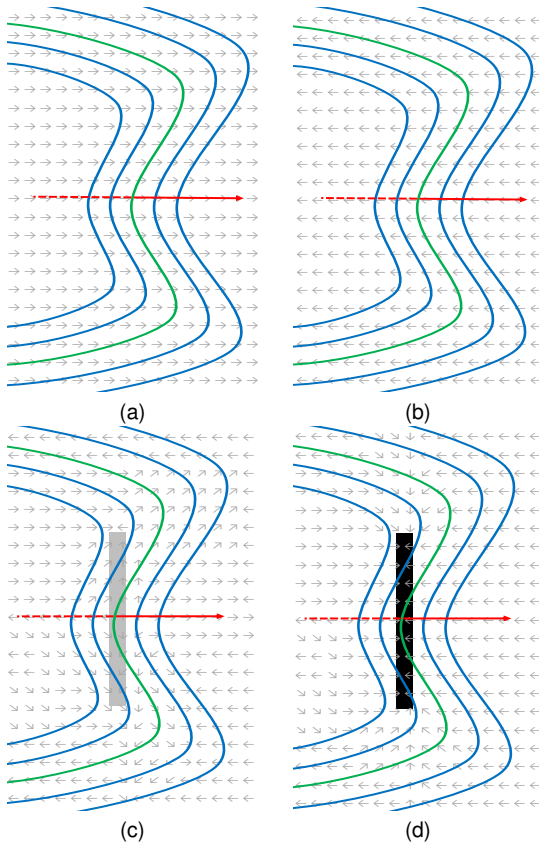
Fig. 4. The normal direction of movement of C for different cases, represented by the red vector. Gray vectors represent the direction of the image's GVF field. Contour C is represented in green, weak edge information is represented by gray pixels and strong edge information is represented by black pixels. (a) The direction of the GVF field is similar to the normal direction of movement of C in a smooth region. (b) The direction of the GVF field is opposite to the normal direction of movement of C in a smooth region. (c) The direction of the GVF field around weak edges. (d) The direction of the GVF field around strong edges.

the compared methods have been tested not only on natural images but also on various medical images [33], [34], [52], [53]. It is also important to note that the energy functional employed in DRLSE comprises the same energy terms as those in our method. The difference is that our method assigns a weight to the length and area terms according to local edge features. Therefore, by comparing our method against DRLSE, we are also confirming the advantages of dynamically weighting these two energy terms during the evolution process according to local edge features.

Five sets of experiments are conducted to evaluate the performance of our proposed method. In all experiments, we set the initial LSF to be a binary function whose values have positive and negative signs inside and outside the initial contour, respectively. Table I shows the parameters used for the edge-based methods evaluated in this work, including our method. Parameters μ, α and λ are constants that determine the influence of the regularization term, area and length terms, respectively. Let us recall that in our proposed method, the influence of the area and length terms is determined by weight $w(\phi, k)$. Note that the sign of α is responsible for inflation (+) or deflation (-) of the contour. Also note that the regularization

term used by PBLS differs from the one used by DRLSE, LSD and our method, thus, the value of μ for PBLS is set to 1, following the author's suggestion in [19].

TABLE I
PARAMETERS USED IN EVALUATED EDGE-BASED METHODS

	μ	α	λ	Δt	Δt_2
LSD	0.2	± 1	1	0.5	-
RD	-	± 1	1	0.8	0.1
DRLSE	0.2	± 3	5	1	-
PBLS	1	± 2	1	-	-
Proposed Method	0.2	-	-	1	-

In all experiments, the detection accuracy of the evaluated methods is measured by the Dice similarity coefficient (DSC) [54] using manually annotated ground truth. The DSC represents the ratio between the intersectional area of A and B and their summation area, i.e.,

$$DSC = \frac{2 |A \cap B|}{|A| + |B|} \tag{13}$$

where A and B represent the segmented region and the ground truth, respectively, and $|\cdot|$ denotes the cardinal of a set. The value of DSC is within the range $[0, 1]$, where 1 indicates perfect overlap and 0 indicates no overlap between A and B.

A. Implementation considerations

The proposed method is implemented using the narrowband approach in order to reduce the computational cost associated with the LSE [2]. This narrowband implementation only requires updating the LSF for each iteration by using a finite difference equation that discretizes the LSE [13]. This is done by defining the LSF, ϕ, on a grid and updating the LSF for each iteration. This update is done on the narrowband, which is also defined on the grid. The narrowband comprises a band of grid points surrounding the evolving contour in both, the outside and inside regions. Specifically, we use a narrowband with a width of k grid points, for both the inside and outside regions of the evolving contour C, in order to be able to define the contours adjacent to C according to the k value in Eq. (9) and Eq. (10). This width remains constant for all iterations, but as C evolves, the area of the narrowband is expected to increase or decrease, if C expands or shrinks, respectively. The narrowband, thus, moves with the evolving contour in each iteration.

Let us denote the discretized form of a time-dependent LSF $\phi(x, y, t)$ by $\phi_{i,j}^\tau$, where (i, j) denotes the spatial position within a grid and τ denotes a discrete time instant. The finite difference equation that implements the LSE is then:

$$\phi_{i,j}^{\tau+1} = \phi_{i,j}^\tau + \Delta t L(\phi_{i,j}^\tau), \ \tau = 0, 1, 2, \dots \tag{14}$$

where Δt denotes a time step, and L is an approximation of the gradient flow in Eq. (12) [55]. As previously stated in Sec. II, term $\omega(\phi, k)$ is regarded as a constant value with respect to time. The computation of $\mathcal{I}(\psi(\phi, k))$ and $\gamma(\psi(\phi, k))$ is also done in a discretized manner within a grid. Let us denote the
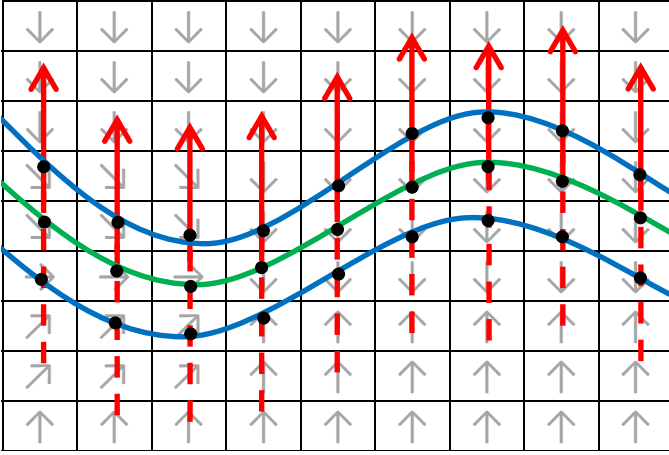
Fig. 5. Example of an LSF defined on a grid. The green line represents the evolving contour C, i.e., the zero level set $\psi(\phi, 0)$. The blue lines represent the contours adjacent to C according to the k value in Eq. (8); in this figure $k = 1$. Edge intensity and GVF field values at the the black points along the adjacent contours are used to compute weighting factor ω in Eq. (7).

discretized zero level set of $\phi(x, y, t)$ at time instant τ by C_τ. The location of C_τ within a grid is used to compute the location of the $2k$ adjacent contours. The line integrals in Eq. (9) and Eq.(10) are then computed in discretized form as a summation over all grid points along the $2k$ adjacent to C_τ, as exemplified in Fig. 5. The resulting value of $\omega(\phi, k)$ at time instant τ is then used to update the LSF for the next iteration, i.e., time instant $\tau + 1$, according to Eq. (14).

B. Analysis of parameter k

The first set of experiments is designed to characterize the effect of parameter k in the boundary detection results and to provide an intuitive interpretation to the tuning of this parameter. Fig. 6 shows the boundary detection results on a synthetic image for different values of k, which results in different values for the weighting term $\omega(\phi, k)$, as the number of contours adjacent to C increases as k increases. It is clear that there is a trade-off between the value of k and the strength of the energy terms, i.e., the area and length terms in Eq. (11). A large value of k implies collecting local edge features in a larger region adjacent to C, which may result in an inaccurate description of this region and thus leakage (see Fig. 6(c)). Smaller values of k may lead to more accurate segmentation results, as this implies collecting local edge features in a region very close to contour C (see Fig. 6(a)). We observe the same behavior when the contour is initialized at different positions, and when the number of iterations varies. Although $k = 1$ usually provides similar results to the ones obtained by using $k = 2$, a value of $k = 1$ may result in a less accurate segmentation than that obtained with a value of $k = 2$ for regions delimited by mostly weak edges. This is due to the fact that a value of $k = 2$ increases the analysis region around the zero level-set. Therefore, in order to increase performance on medical images with weak edges, we set $k = 2$ in the remaining experiments to avoid leakages while increasing the analysis region around the zero level-set.
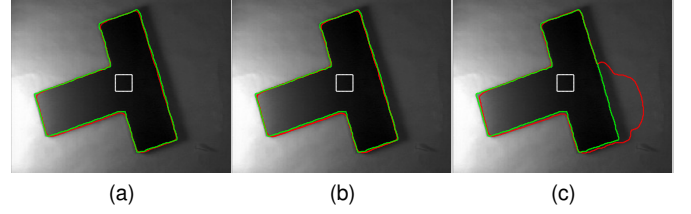

Fig. 6. Boundary detection results of the proposed method on a synthetic image with 120 iterations and different values for parameter k. (a) $k = 2$ (DSC=0.9802). (b) $k = 3$ (DSC=0.9798). (c) $k = 6$ (DSC=0.8057). White curves denote the initial contour; red curves denote the final contour, and green curves denotes the ground truth.

C. Results on real medical images

The second set of experiments evaluates the proposed method on real medical images and compares it with LSD, RD and DRLSE. This experiment is divided in two parts. In Part 1, the number of iterations for all evaluated methods is set to the number required to achieve convergence by our method. In Part 2, we increase the number of iterations used in Part 1 in order to evaluate the accuracy of LSD, RD and DRLSE as the number of iterations in Part 1 increases. Table II tabulates the DSC values for different regions of MRI and CT slices. Experiments 1-15 represent different regions of different MRI slices of a spinal cord (vertebral body, sagittal view), Experiments 16 represents a region of an MRI slice of a brain (the caudate nucleus is the object to be segmented), Experiments 17 and 18 represent two regions of an MRI slice of a pelvis; Experiments 19 and 20 represent two regions of a CT slice of a skull, Experiments 21-28 represent different regions of MRI slices of lumbar discs, and Experiments 29-30 represent different regions of two different MRI slices of a spinal cord (spinous process, sagittal view). Experiments 21-28 represent very challenging cases where the target regions have intensities very similar to those of the surrounding regions, thus making it difficult to clearly delineate the objects' boundaries.

Results in Table II show that our approach achieves the highest accuracy for the majority of experiments. The methods whose results are underlined in Table II, Part 1, achieve convergence before the proposed method and thus remain stable as the algorithms iterate further. In Experiments 2, 14-17, Part 1, and Experiments 11, 13, 15, 17, Part 2, the other evaluated methods achieve higher DSC values than our method. In the case of Experiment 2, Part 1, RD does not converge in the tabulated number of iterations, and more iterations cause significant leakage in Part 2. In the case of Experiments 14-17, Part 1, DRLSE achieves convergence before our proposed method (underlined results), thus resulting in higher DSC values. For the case of Experiments 14 and 16, after increasing the number of iterations in Part 2, our method achieves higher DSC values. Our method, in these two cases, requires a larger number of iterations than DRLSE to accurately detect the desired boundary. In the case of Experiments 15 and 17, Part 2, DRLSE outperforms our method by only 0.670%. For Experiments 11,13, Part 2, RD also outperforms our method by only 0.004%. It is also important to note that RD and LSD

Fig. 7. Visual results attained by LSD, RD, DRLSE and our proposed method, for Part 1 experiments.The white curves denote the initial contours, the red curves represent the final contour, and the green curves represent the ground truth. For Experiments 27 & 28, the first line of DSC values is for the cecum region (upper region - Experiment 27), while the second line is for the sacrum region (bottom region - Experiment 28).

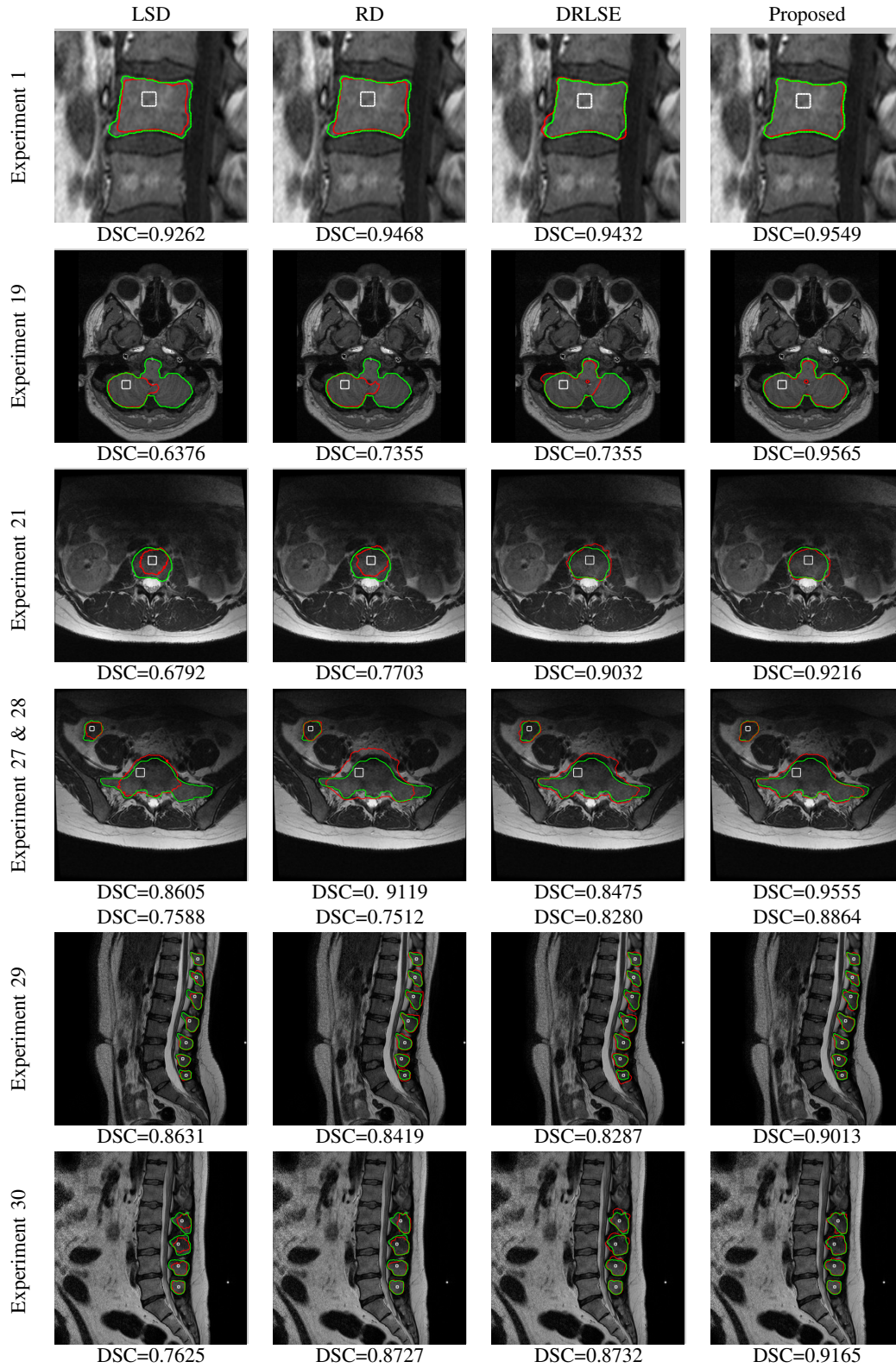Fig. 8. Visual results attained by LSD, RD, DRLSE and our proposed method, for Part 2 experiments. The white curves denote the initial contours, the red curves represent the final contour, and the green curves represent the ground truth. For Experiments 27 & 28, the first line of DSC values is for the cecum region (upper region - Experiment 27), while the second line is for the sacrum region (bottom region - Experiment 28).
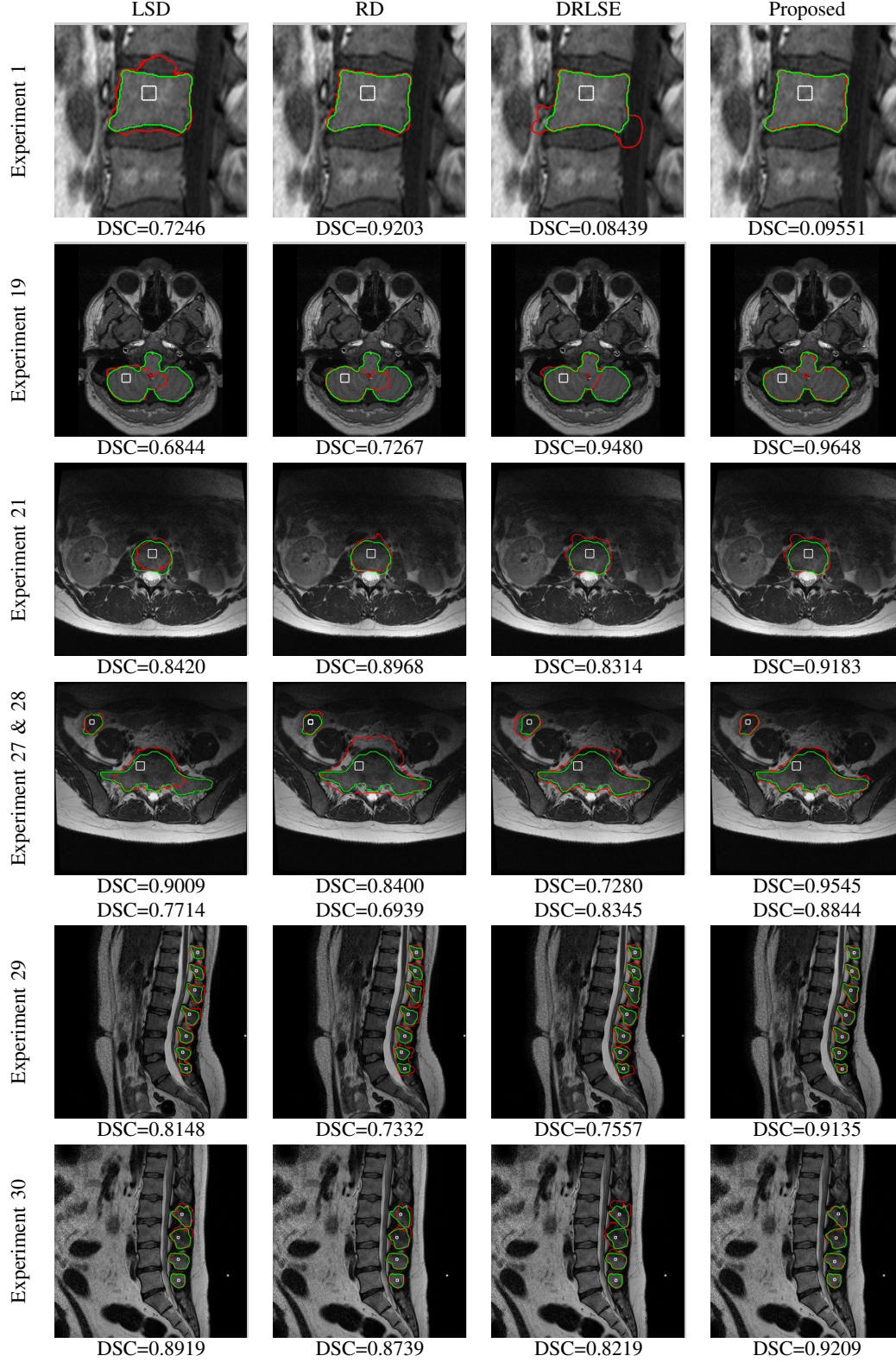
TABLE II
SEGMENTATION ACCURACY OF VARIOUS LEVEL SET METHODS FOR REAL MEDICAL IMAGES.

Exp.	Part 1					Part 2				
	DSC				No. iterations	DSC				No. iterations
	LSD	RD	DRLSE	Proposed approach		LSD	RD	DRLSE	Proposed approach	
1	0.9262	0.9468	0.9432	**0.9549**	50	0.7246	0.9203	0.8438	**0.9551**	80
2	0.9370	**0.9437**	0.9016	0.9315	50	0.7868	0.5297	0.8913	**0.9247**	100
3	0.9451	0.9679	0.9501	**0.9686**	50	0.6873	0.5651	0.6082	**0.9686**	100
4	0.9391	0.9560	0.9311	**0.9595**	50	0.7638	0.8676	0.8741	**0.9590**	60
5	0.9368	0.9603	<u>0.9552</u>	**0.9636**	50	0.5563	0.9277	0.9544	**0.9617**	100
6	0.8814	0.9254	0.9166	**0.9340**	50	0.7695	0.8940	0.8205	**0.9352**	100
7	0.9085	0.9330	0.9412	**0.9589**	50	0.7233	0.4730	0.9397	**0.9582**	100
8	0.9417	0.8375	0.9165	**0.9543**	50	0.7041	0.8200	0.7235	**0.9538**	100
9	0.8128	0.8234	<u>0.9445</u>	**0.9472**	50	0.9364	0.9422	0.9461	**0.9479**	100
10	0.9070	0.8745	<u>0.9332</u>	**0.9468**	50	0.8609	0.9067	0.9335	**0.9468**	100
11	0.8821	0.8944	<u>0.9420</u>	**0.9484**	50	0.9218	**0.9541**	0.9434	0.9487	100
12	0.7934	0.8006	0.8123	**0.9565**	50	0.9055	0.8176	0.8152	**0.9569**	100
13	0.7150	0.7081	0.9526	**0.9674**	50	0.7392	**0.9560**	0.9252	0.9538	100
14	0.8875	0.9058	<u>**0.9463**</u>	0.9443	50	0.9015	0.9437	0.9466	**0.9500**	100
15	0.8496	0.7589	<u>**0.9577**</u>	0.9444	50	0.9466	0.9527	**0.9571**	0.9482	100
16	0.9584	0.7747	<u>**0.9764**</u>	0.9670	50	0.7848	0.9507	0.9776	**0.9791**	100
17	0.9397	0.7643	<u>**0.9641**</u>	0.9516	50	0.6591	0.9294	0.9767	**0.9727**	100
18	0.8643	0.8794	0.8510	**0.9157**	50	0.8076	0.8379	0.8510	**0.9157**	100
19	0.6376	0.6416	0.7355	**0.9565**	100	0.6844	0.7267	0.9480	**0.9648**	140
20	0.7095	0.7388	0.9273	**0.9632**	100	0.7971	0.8418	0.8680	**0.9632**	140
21	0.6792	0.7703	0.8874	**0.9216**	60	0.7812	0.8837	0.8314	**0.9183**	80
22	0.8504	0.8371	0.9032	**0.9290**	60	0.8603	0.8581	0.8877	**0.9270**	80
23	0.6527	0.7080	0.9182	**0.9389**	60	0.7004	0.8524	0.8968	**0.9372**	80
24	0.9057	0.8907	0.8920	**0.9406**	60	0.8852	0.8697	0.8816	**0.9361**	80
25	0.5701	0.6172	0.8365	**0.9385**	60	0.6122	0.6472	0.9099	**0.9319**	80
26	0.6824	0.7349	0.8174	**0.9598**	70	0.7014	0.8119	0.8331	**0.9462**	90
27	0.8605	0.9119	0.8475	**0.9555**	50	0.9009	0.8400	0.7280	**0.9545**	80
28	0.7588	0.7512	0.8280	**0.8864**	100	0.7714	0.6939	0.8345	**0.8844**	130
29	0.8631	0.8419	0.8287	**0.9013**	60	0.8148	0.7332	0.7557	**0.9135**	100
30	0.7625	0.8727	0.8732	**0.9165**	60	0.8919	0.8739	0.8219	**0.9209**	100

tend to result in leakage as the number of iteration increases; see for example Experiments 2, 3 and 4, Part 2. For the challenging cases (Experiments 21-28), our method achieves convergence before the other evaluated methods and results in higher DSC values. For Experiments 29-30, the regions we intend to delineate are delimited by weak edges. LSD, RD and DRLSE do not converge in the tabulated number of iterations in Part 1 and consequently, tend to result in significant leakage as the number of iteration increases in Part 2. The DSC values attained for these experiments show that the proposed method is also capable to outperform the other methods for these images.

It is important to mention that leakage in DRLSE may be the result of the distance regularization term and area term forcing the zero level set to continue to evolve when the zero level set is already at the desired boundary. Even though our proposed method also employs the distance regularization employed by DRLSE, it prevents leakage and achieves convergence by weighting the $Length_2$ and $Area_2$ terms according to local edge features. This confirms the advantage of our weighting approach.

Visual results for Part 1 experiments are shown in Fig. 7. Note that the images in the depicted experiments contain several intensity inhomogeneities. The third and fourth rows represent challenging cases where the target objects have intensities very similar to the surrounding regions. It can be seen that our method is capable of detecting regions delineated by weak edges. The other evaluated methods (see Columns 1-3 of Fig. 7), fail to correctly segment the regions for the same number of iterations required by our method. Although RD and DRLSE attain an accuracy similar to that obtained by our method for Experiment 1, these methods fail when they are allowed to iterate further, as shown in Fig. 8. Among the most challenging regions are those in Experiment 27 and 28 (fourth row of Fig. 7). In this case, our method successfully detects the cecum region (Experiment 27). This region is characterized by very weak edges. Note that all methods fail to correctly detect the upper edge of the sacrum region (Experiment 28). However, our method is the one that results in the least amount of leakage and thus, the highest DCS value.

Visual results for Part 2 experiments are shown in Fig. 8. Note that the other evaluated methods results in significant leakage when they iterate further. These visual results confirm that taking into account the amount of edge information and the direction of the image's GVF field in the adjacent region located inside and outside of the evolving contour to

control the influence of various energy terms, can improve segmentation accuracy and minimize leakage.

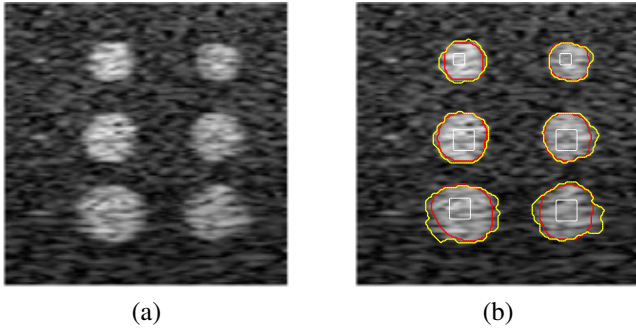### D. Comparisons to PBLS

(a)   (b)

Fig. 9. (a) Synthetic phantom. The three circles in each column, from top to bottom, have a radius of 17, 20, and 23 pixels, respectively. (b) Contours obtained by PBLS (yellow) and our proposed method (red). The white curves denote the initial contours.
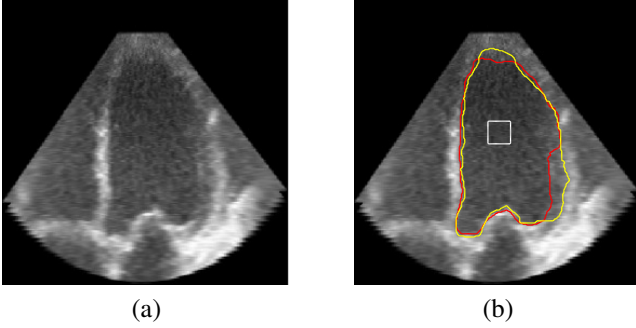

(a)   (b)

Fig. 10. (a) Ultrasound image of the left ventricle of the heart. (b) Contours obtained by PBLS (yellow) and our proposed method (red). The white curve denotes the initial contour.

The third set of experiments compares our method to PBLS on synthetic images and real ultra sound images. PBLS has been shown to perform very well in the presence of weak edges. PBLS uses a similar alignment term as the one proposed by Kimmel's method. Fig. 9 and Fig. 10 show visual results attained by PBLS and the proposed method on a synthetic and ultra sound image, respectively. Note that both of these images depict very weak edges and high levels of noise. For the case of PBLS, we use the parameters that provide the best edge map for each image. From Fig. 9, we observe that the contours produced by PBLS tend to cover more area of the synthetic circles than the proposed method. This is due to the phase-based edge indicator used by PBLS to detect the edges. However, the proposed method attains very competitive results in the ultra sound image depicted in Fig. 10. It is interesting to note that our proposed method tends to stop at the very weak edge depicted in the lower right part of the ventricle of Fig. 10,while PBLS tends to stop at the stronger edge. This is expected, as our proposed method averages edge features over k contours adjacent to the evolving contour, which helps evolving contour to conform to very weak edges.

Fig. 11 shows visual results and DSC values attained by PBLS and our proposed method in more challenging ultra-sound images. Note that our method attains very competitive

results for the regions of Fig. 11 (a)-(d), while it outperforms PBLS for the regions of Fig. 11 (e)-(h).

PBLS   Proposed

(a) DSC=0.9227   (b) DSC=0.9268

(c) DSC=0.9445   (d) DSC=0.9593

(e) DSC=0.8666   (f) DSC=0.9298
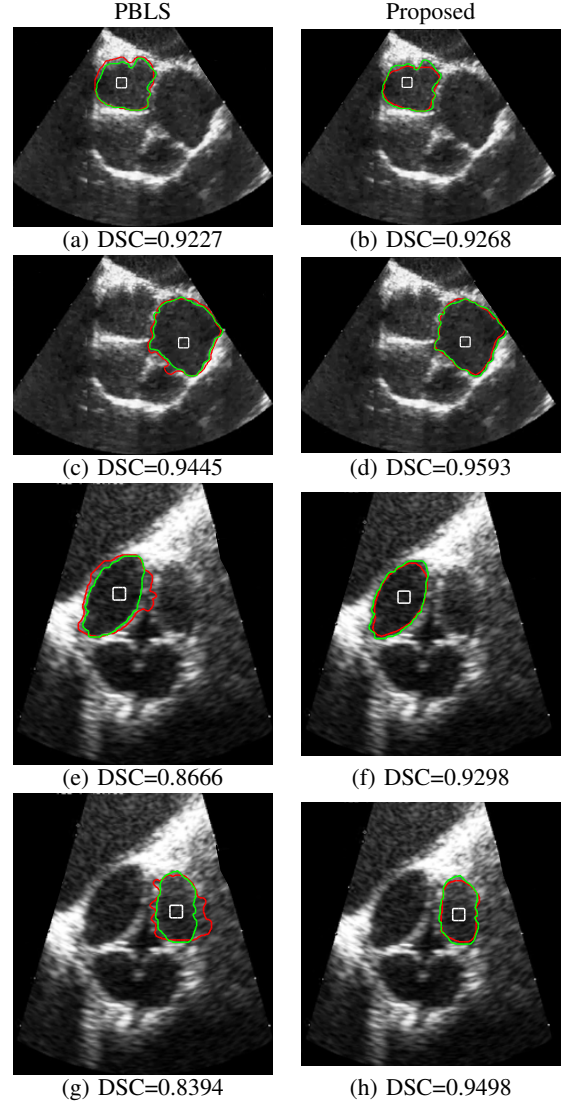
(g) DSC=0.8394   (h) DSC=0.9498

Fig. 11. Visual results and DSC values attained by PBLS and the proposed method in ultra sound images of the heart. Each row corresponds to a region. The white curves denote the initial contours, the red curves represent the final contour and the green curves represent the ground truth.

E. Comparisons to region-based active contours

The fourth set of experiments compares our method to Kimmel's method on synthetic images and real medical images. Let us recall that Kimmel's method is a region-based method. It is important to mention that region-based methods are usually based on the Mumford-Shah functional [56]. For example, the method of active contours without edges (Chan-Vese model) solves the piecewise constant Mumford-Shah model but restricts the solution to be a piecewise constant solution with only two constants [6]. Other proposals have successfully solved the energy minimization problem proposed by Mumford and Shah by convex optimization, such as those by Cai, Chan et al. [57], [58].

Visual results and DSC values for Kimmel's method and the proposed method are shown in Fig. 12. These results

(a) DSC=0.9629 (b) DSC=0.5780 (c) DSC=0.6392 (d) DSC=0.0001

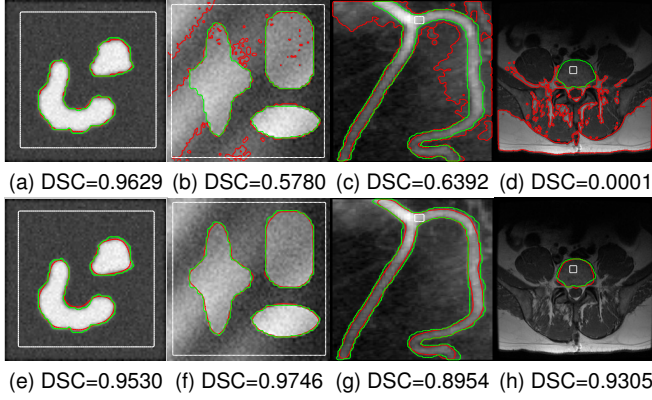(e) DSC=0.9530 (f) DSC=0.9746 (g) DSC=0.8954 (h) DSC=0.9305

Fig. 12. Visual results and DSC values for synthetic images (columns 1 and 2) and real medical images (columns 3 and 4). The first row corresponds to Kimmel's method, while the second row corresponds to our method. Column 3 depicts a X-ray vessel image, and column 4 depicts an MRI slice of an abdominal axial cross sectional view of the human body. The white curves denote the initial contours, the red curves represent the final contour and the green curves represent the ground truth.

show that Kimmel's method outperforms ours for the synthetic image in Fig. 12 (a). This is mainly due to the fact that Kimmel's method incorporates a region-based force into the model, which increases accuracy when two regions can be easily detected in the image. Our method, however, attains a very similar DSC value to that attained by Kimmel's in this image. For cases where no two regions can be easily detected, Kimmel's method is outperformed by ours. This is evidenced in the synthetic image in Fig. 12 (b), where it is difficult to delineate two regions due to the weak edges and the intensity inhomogeneities. Similar results are obtained for the real medical images in Fig. 12 (c) and (d). Our method achieves higher DCS values for these images. It is interesting to note the performance of Kimmel's method on the image in Fig. 12 (d). As mentioned before, this method attempts to detect two homogeneous regions. Therefore, the detected two regions in this case correspond to those that appear to be the most similar regions in terms of intensities.

F. Sensitivity to position of initial contour

The last set of experiments evaluates the sensitivity to the initial contour's position of the edge-based methods tabulated in Table II. To this end, we employ different positions for the initial contour on synthetic images and real medical images. Visual results and DSC values are shown in Fig. 13 and 14. All methods have been evaluated with the same number of iterations. In Fig. 13, we show results for a noisy synthetic image. In this case, we tested the case of initializing the contour inside and outside the target regions. These results show that our method successfully detects the objects' boundary even when the position of the initial contour is located outside the target regions. Our method also achieves the highest DSC values. Fig. 14 demonstrates the robustness of the proposed method with different initial contours on a real medical image. In this case, RD performs better than LSD and DRLSE, as it is capable to conform to most of the desired

boundary regardless of the position of the initial contour. LSD particularly fails when the initial contour is located close to a weak boundary. Our method successfully conforms to the desired boundary with high accuracy for all initialization positions. It is interesting to see that the proposed method results in very similar DSC values for this medical image regardless the position of the initial contour. This confirms the effectiveness of weight ω in our method to control the influence of forces according to local features.

(a) DSC=0.8621 (b) DSC=0.9364 (c) DSC=0.9518 (d) DSC=0.9746

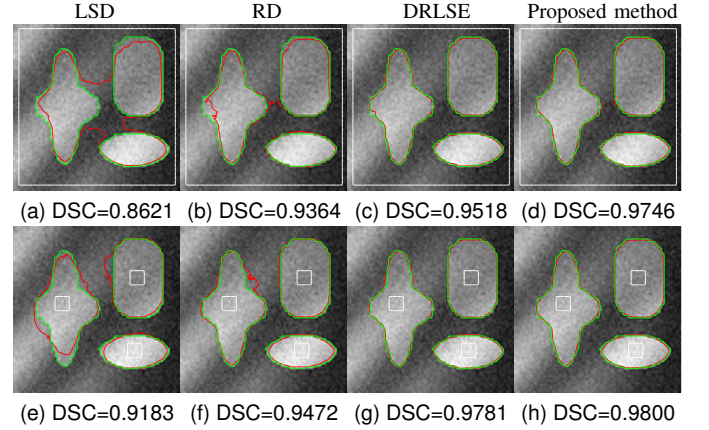(e) DSC=0.9183 (f) DSC=0.9472 (g) DSC=0.9781 (h) DSC=0.9800

Fig. 13. Segmentation results on a synthetic image after 100 iterations using different positions for the initial contour. The white curves denote the initial contours, the red curves represent the final contour and the green curves represent the ground truth. Each row shows results for a different initial position.

(a) DSC=0.7780 (b) DSC=0.9284 (c) DSC=0.8938 (d) DSC=0.9562

(e) DSC=0.7677 (f) DSC=0.8842 (g) DSC=0.7303 (h) DSC=0.9577

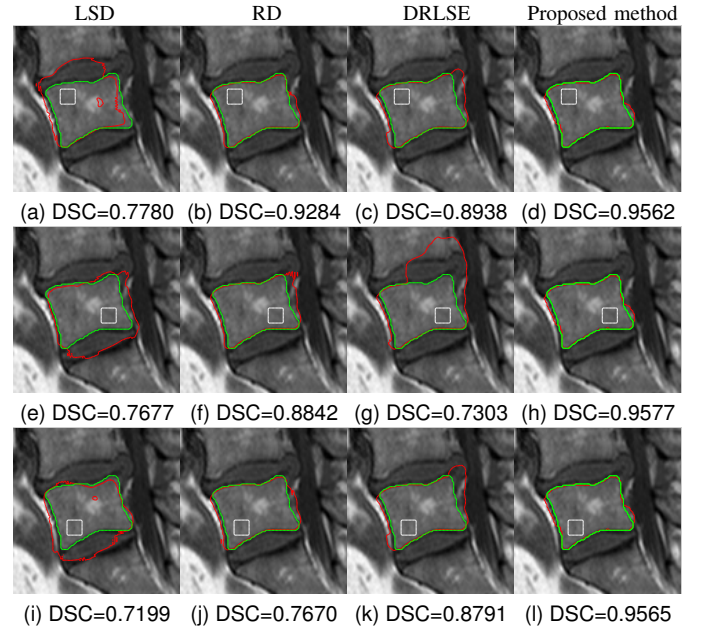(i) DSC=0.7199 (j) DSC=0.7670 (k) DSC=0.8791 (l) DSC=0.9565

Fig. 14. Segmentation results on a MRI slice of a spinal cord (vertebral body, sagittal view) after 50 iterations using different positions for the initial contour. The white curves denote the initial contours, the red curves represent the final contour and the green curves represent the ground truth. Each row shows results for a different initial position.

G. Computational complexity

We finish this section with some comments about the computational complexity of the proposed method. Despite

the advantages of the narrowband implementation, the computational cost of our method increases with respect to that of the other evaluated methods. This is mainly due to the fact that the proposed method collects local edge features from a number of contours adjacent to the evolving contour C, at each iteration.

We record the CPU time during the experiments. All methods are implemented in Matlab 8.4 and run on a computer with Intel (R) Core (TM) i5 CPU, 3.20 GHz, 16 GB RAM, with Windows 7. The average CPU time of the 30 experiments tabulated in Part 1 of Table II, are 10.41 seconds, 9.57 seconds, 19.55 seconds and 27.12 seconds for LSD, RD, DRLSE and the proposed method, respectively. Although LSD and RD attain lower average CPU times than those attained by DRLSE, the accuracy of these methods is, overall, lower than that of DRLSE. As expected, the proposed method takes longer CPU times to detect boundaries. However, these times may be easily reduced by introducing optimizations to the implementation code.

IV. CONCLUSIONS

In this paper we proposed a novel medical image segmentation method based on a level set active contour model that provides improved boundary detection accuracy around weak edges. The method uses a weighting factor to leverage the advantages of incorporating local edge features into the objective energy functional. Specifically, the method combines edge intensity information with edge directional information collected from the adjacent region located inside and outside of the evolving contour. This information is then used to determine the importance of various energy terms in an energy functional. As a consequence, the proposed method is able to accurately drive the contour to the desired boundary even around weak edges, thus minimizing leakages in medical images. The performance of the proposed method was demonstrated on various real medical images and compared with the performance of various edge-based and region-based methods. Experimental results showed that the proposed method outperforms other state-of-the-art edge-based level-set approaches, in terms of segmentation accuracy, and is capable to converge to the desired boundary in less iterations. Our future work will focus on extending the proposed method to 3D images.

REFERENCES

[1] V. Caselles, R. Kimmel, and G. Sapiro, "Geodesic active contours," *International Journal of Computer Vision*, vol. 22, no. 1, pp. 61–79, 1997.

[2] C. Li, C. Xu, C. Gui, and M. D. Fox, "Level set evolution without re-initialization: a new variational formulation," in *Proceedings of IEEE Computer Society Conference on Computer Vision and Pattern Recognition*, vol. 1. IEEE, 2005, pp. 430–436.

[3] S. C. Zhu and A. Yuille, "Region competition: Unifying snakes, region growing, and bayes/mdl for multiband image segmentation," *IEEE Transactions on Pattern Analysis and Machine Intelligence*, vol. 18, no. 9, pp. 884–900, 1996.

[4] R. Wilson and C.-T. Li, "A class of discrete multiresolution random fields and its application to image segmentation," *IEEE Transactions on Pattern Analysis and Machine Intelligence*, vol. 25, no. 1, pp. 42–56, 2003.

[5] C.-T. Li, "Multiresolution image segmentation integrating gibbs sampler and region merging algorithm," *Signal Processing*, vol. 83, no. 1, pp. 67–78, 2003.

[6] T. F. Chan and L. A. Vese, "Active contours without edges," *IEEE Transactions on Image Processing*, vol. 10, no. 2, pp. 266–277, 2001.

[7] C. Li, C.-Y. Kao, J. C. Gore, and Z. Ding, "Implicit active contours driven by local binary fitting energy," in *Proceedings of IEEE Conference on Computer Vision and Pattern Recognition*, 2007, pp. 1–7.

[8] X. Xie, "Active contouring based on gradient vector interaction and constrained level set diffusion," *IEEE Transactions on Image Processing*, vol. 19, no. 1, pp. 154–164, 2010.

[9] C. Li, C.-Y. Kao, J. C. Gore, and Z. Ding, "Minimization of region-scalable fitting energy for image segmentation," *IEEE Transactions on Image Processing*, vol. 17, no. 10, pp. 1940–1949, 2008.

[10] L. A. Vese and T. F. Chan, "A multiphase level set framework for image segmentation using the mumford and shah model," *International journal of computer vision*, vol. 50, no. 3, pp. 271–293, 2002.

[11] K. Zhang, H. Song, and L. Zhang, "Active contours driven by local image fitting energy," *Pattern recognition*, vol. 43, no. 4, pp. 1199–1206, 2010.

[12] K. Zhang, D. Zhang, and S. Zhang, "A variational multiphase level set approach to simultaneous segmentation and bias correction," in *Proceedings of IEEE International Conference on Image Processing (ICIP)*, 2010, pp. 4105–4108.

[13] C. Li, C. Xu, C. Gui, and M. D. Fox, "Distance regularized level set evolution and its application to image segmentation," *IEEE Transactions on Image Processing*, vol. 19, no. 12, pp. 3243–3254, 2010.

[14] X. Zhao, Y. Wang, and G. Jozsef, "Robust shape-constrained active contour for whole heart segmentation in 3D CT images for radiotherapy planning," in *IEEE International Conference on Image Processing*. IEEE, 2014, pp. 1–5.

[15] K. Q. Tao, Z. Qu, and D. D. Wang, "Lung CT image segmentation based on mixture active contour model," in *Applied Mechanics and Materials*, vol. 618. Trans Tech Publ, 2014, pp. 405–409.

[16] H. T. Huynh, I. Karademir, A. Oto, and K. Suzuki, "Liver volumetry in mri by using fast marching algorithm coupled with 3D geodesic active contour segmentation," in *Computational Intelligence in Biomedical Imaging*. Springer, 2014, pp. 141–157.

[17] S. C. Agner, J. Xu, and A. Madabhushi, "Spectral embedding based active contour (seac) for lesion segmentation on breast dynamic contrast enhanced magnetic resonance imaging," *Medical physics*, vol. 40, no. 3, pp. 032–305, 2013.

[18] H. Hu, H. Liu, Z. Gao, and L. Huang, "Hybrid segmentation of left ventricle in cardiac mri using gaussian-mixture model and region restricted dynamic programming," *Magnetic resonance imaging*, vol. 31, no. 4, pp. 575–584, 2013.

[19] A. Belaid, D. Boukerroui, Y. Maingourd, and J.-F. Lerallut, "Phase-based level set segmentation of ultrasound images," *IEEE Transactions on Information Technology in Biomedicine*, vol. 15, no. 1, pp. 138–147, 2011.

[20] Z. Ji, Y. Xia, Q. Sun, G. Cao, and Q. Chen, "Active contours driven by local likelihood image fitting energy for image segmentation," *Information Sciences*, vol. 301, pp. 285–304, 2015.

[21] Y. Zhou, W.-R. Shi, W. Chen, Y.-l. Chen, Y. Li, L.-W. Tan, and D.-Q. Chen, "Active contours driven by localizing region and edge-based intensity fitting energy with application to segmentation of the left ventricle in cardiac ct images," *Neurocomputing*, vol. 156, pp. 199–210, 2015.

[22] S. Osher and J. A. Sethian, "Fronts propagating with curvature-dependent speed: algorithms based on hamilton-jacobi formulations," *Journal of Computational Physics*, vol. 79, no. 1, pp. 12–49, 1988.

[23] D. Peng, B. Merriman, S. Osher, H. Zhao, and M. Kang, "A PDE-based fast local level set method," *Journal of Computational Physics*, vol. 155, no. 2, pp. 410–438, 1999.

[24] J. Weickert and G. Kühne, *Fast methods for implicit active contour models*. Springer, 2003.

[25] R. Malladi, J. A. Sethian, and B. C. Vemuri, "Shape modeling with front propagation: A level set approach," *IEEE Transactions on Pattern Analysis and Machine Intelligence*, vol. 17, no. 2, pp. 158–175, 1995.

[26] B. Vemuri and Y. Chen, "Joint image registration and segmentation," in *Geometric level set methods in imaging, vision, and graphics*. Springer, 2003, pp. 251–269.

[27] R. Kimmel and A. Bruckstein, "On edge detection, edge integration and geometric active contours," in *Proceedings of ISMM*, vol. 3, 2002, pp. 37–45.

[28] R. Kimmel and A. M. Bruckstein, "Regularized laplacian zero crossings as optimal edge integrators," *International Journal of Computer Vision*, vol. 53, no. 3, pp. 225–243, 2003.

[29] R. Kimmel, "Fast edge integration," in *Geometric Level Set Methods in Imaging, Vision, and Graphics*. Springer, 2003, pp. 59–77.

[30] A. Vasilevskiy and K. Siddiqi, "Flux maximizing geometric flows," *IEEE Transactions on Pattern Analysis and Machine Intelligence*, vol. 24, no. 12, pp. 1565–1578, 2002.

[31] V. Estellers, D. Zosso, X. Bresson, and J.-P. Thiran, "Harmonic active contours," *IEEE Transactions on Image Processing*, vol. 23, no. 1, pp. 69–82, 2014.

[32] K. Zhang, L. Zhang, H. Song, and D. Zhang, "Reinitialization-free level set evolution via reaction diffusion," *IEEE Transactions on Image Processing*, vol. 22, no. 1, pp. 258–271, 2013.

[33] L. Jin-qing and L. Wei-wei, "Adaptive medical image segmentation algorithm combined with drlse model," *Procedia Engineering*, vol. 15, pp. 2634–2638, 2011.

[34] I. Rianto and P. Pranowo, "Distance regularized level set evolution for medical image segmentation," in *The 1st Conference on Information Technology, Computer, and Electrical Engineering (CITACEE)*, vol. 1. Department of Computer Engineering, 2013, pp. 49–51.

[35] P. H. Lim, U. Bagci, and L. Bai, "Introducing willmore flow into level set segmentation of spinal vertebrae," *IEEE Transactions on Biomedical Engineering*, vol. 60, no. 1, pp. 115–122, 2013.

[36] Y. Li, W. Liang, Y. Zhang, H. An, and J. Tan, "Automatic lumbar vertebrae detection based on feature fusion deep learning for partial occluded c-arm x-ray images," in *IEEE 38th Annual International Conference of the Engineering in Medicine and Biology Society (EMBC)*. IEEE, 2016, pp. 647–650.

[37] P. H. Lim, U. Bagci, O. Aras, Y. Wang, and L. Bai, "A novel spinal vertebrae segmentation framework combining geometric flow and shape prior with level set method," in *2012 9th IEEE International Symposium on Biomedical Imaging (ISBI)*. IEEE, 2012, pp. 1703–1706.

[38] A. H. Zhuang, D. J. Valentino, and A. W. Toga, "Skull-stripping magnetic resonance brain images using a model-based level set," *NeuroImage*, vol. 32, no. 1, pp. 79–92, 2006.

[39] H. Rifai, I. Bloch, S. Hutchinson, J. Wiart, and L. Garnero, "Segmentation of the skull in mri volumes using deformable model and taking the partial volume effect into account," *Medical image analysis*, vol. 4, no. 3, pp. 219–233, 2000.

[40] J. Huang, F. Jian, H. Wu, and H. Li, "An improved level set method for vertebra ct image segmentation," *Biomedical engineering online*, vol. 12, no. 1, p. 1, 2013.

[41] N. Jafarian, K. Kazemi, H. A. Moghaddam, R. Grebe, M. Fournier, M. S. Helfroush, C. Gondry-Jouet, and F. Wallois, "Automatic segmentation of newborns skull and fontanel from ct data using model-based variational level set," *Signal, Image and Video Processing*, vol. 8, no. 2, pp. 377–387, 2014.

[42] S. Ghadimi, H. A. Moghaddam, R. Grebe, and F. Wallois, "Skull segmentation and reconstruction from newborn ct images using coupled level sets," *IEEE journal of biomedical and health informatics*, vol. 20, no. 2, pp. 563–573, 2016.

[43] W. Wang, L. Zhu, J. Qin, Y.-P. Chui, B. N. Li, and P.-A. Heng, "Multiscale geodesic active contours for ultrasound image segmentation using speckle reducing anisotropic diffusion," *Optics and Lasers in Engineering*, vol. 54, pp. 105–116, 2014.

[44] M. M. Abdelsamea, G. Gnecco, and M. M. Gaber, "An efficient self-organizing active contour model for image segmentation," *Neurocomputing*, vol. 149, no. 9, pp. 820–835, 2014.

[45] A. Khadidos, V. Sanchez, and C.-T. Li, "Active contours based on weighted gradient vector flow and balloon forces for medical image segmentation," in *IEEE International Conference on Image Processing*. IEEE, 2014, pp. 902–906.

[46] G. Zhu, S. Zhang, Q. Zeng, and C. Wang, "Gradient vector flow active contours with prior directional information," *Pattern Recognition Letters*, vol. 31, no. 9, pp. 845–856, 2010.

[47] S. Lankton and A. Tannenbaum, "Localizing region-based active contours," *IEEE Transactions on Image Processing*, vol. 17, no. 11, pp. 2029–2039, 2008.

[48] M. Jung, G. Peyré, and L. D. Cohen, "Nonlocal active contours," *SIAM Journal on Imaging Sciences*, vol. 5, no. 3, pp. 1022–1054, 2012.

[49] S. Candemir and Y. S. Akgül, "Adaptive regularization parameter for graph cut segmentation," in *International Conference Image Analysis and Recognition*. Springer, 2010, pp. 117–126.

[50] C. Yu, W. Zhang, Y. Yu, and Y. Li, "A novel active contour model for image segmentation using distance regularization term," *Computers & Mathematics with Applications*, vol. 65, no. 11, pp. 1746–1759, 2013.

[51] K. B. Prakash, S. Zhou, T. C. Morgan, D. F. Hanley, and W. L. Nowinski, "Segmentation and quantification of intra-ventricular/cerebral hemorrhage in CT scans by modified distance regularized level set evolution technique," *International journal of computer assisted radiology and surgery*, vol. 7, no. 5, pp. 785–798, 2012.

[52] A. Belaid, D. Boukerroui, Y. Maingourd, and J.-F. Lerallut, "Implicit active contours for ultrasound images segmentation driven by phase information and local maximum likelihood," in *2011 IEEE international symposium on biomedical imaging: from nano to macro*. IEEE, 2011, pp. 630–635.

[53] S. Prabha, K. Anandh, C. Sujatha, and S. Ramakrishnan, "Total variation based edge enhancement for level set segmentation and asymmetry analysis in breast thermograms," in *2014 36th Annual International Conference of the IEEE Engineering in Medicine and Biology Society*. IEEE, 2014, pp. 6438–6441.

[54] L. R. Dice, "Measures of the amount of ecologic association between species," *Ecology*, vol. 26, no. 3, pp. 297–302, 1945.

[55] G. Aubert and P. Kornprobst, "Mathematical problems in image processing: Partial differential equations and the calculus of variations," *Applied Mathematical Sciences*, 2002.

[56] D. Mumford and J. Shah, "Optimal approximations by piecewise smooth functions and associated variational problems," *Communications on pure and applied mathematics*, vol. 42, no. 5, pp. 577–685, 1989.

[57] X. Cai, R. Chan, and T. Zeng, "A two-stage image segmentation method using a convex variant of the mumford–shah model and thresholding," *SIAM Journal on Imaging Sciences*, vol. 6, no. 1, pp. 368–390, 2013.

[58] X. Cai, R. Chan, and T. Zeng, "Image segmentation by convex approximation of the mumford–shah model," *UCLA CAM Report*, pp. 12–20, 2012.

PLACE
PHOTO
HERE

Alaa Khadidos received the B.S. degree from King Abdulaziz University, Jeddah, Saudi Arabia, in 2006, the M.Sc. degree from the The University of Birmingham, Birmingham, United Kingdom, in 2011, and the Ph.D. degree from the University of Warwick, Coventry, United Kingdom, in 2017, all in computer science. He is currently an Assistant Professor with the Faculty of Computing and Information Technology, King Abdulaziz University, Jeddah, Saudi Arabia. His main research interests include the areas of computer vision, machine learning, optimization, and medical image analysis.

Victor Sanchez received his M.Sc. degree in 2003 from the University of Alberta, Canada, and his Ph.D. in 2010 from the University of British Columbia, Canada. He is currently an Associate Professor at the Department of Computer Science, University of Warwick, UK. From 2011 to 2012, he was with the Video and Image Processing (VIP) Lab, University of California, Berkeley, as a post-doctoral researcher. In 2012, he was a visiting lecturer at the Group on Interactive Coding of Images, Universitat Autnoma de Barcelona. Dr Sanchez main research interests are in the area of signal and information processing with applications to multimedia analysis, image and video coding and communications. He has published several technical papers in these areas and co-authored a book (Springer, 2012). His research has been funded by Consejo Nacional de Ciencia y Tecnologia, Mexico, the Natural Sciences and Engineering Research Council of Canada, the Canadian Institutes of Health Research, the FP7 and H2020 programs of the European Union, and the Engineering and Physical Sciences Research Council, UK.

Chang-Tsun Li Chang-Tsun Li received the BEng degree in electrical engineering from National Defence University (NDU), Taiwan, in 1987, the MSc degree in computer science from U.S. Naval Postgraduate School, USA, in 1992, and the PhD degree in computer science from the University of Warwick, UK, in 1998. He was an associate professor of the Department of Electrical Engineering at NDU during 1998-2002 and a visiting professor of the Department of Computer Science at U.S. Naval Postgraduate School in the second half of 2001. He was a professor of the Department of Computer Science at the University of Warwick, UK, until Dec 2016. He is currently a professor of the School of Computing and Mathematics, Charles Sturt University, Australia. His research interests include multimedia forensics and security, biometrics, data mining, machine learning, data analytics, computer vision, image processing, pattern recognition, bioinformatics, and content-based image retrieval. He is currently Associate Editor of the EURASIP Journal of Image and Video Processing (JIVP) and Associate of Editor of IET Biometrics. He has involved in the organisation of a number of international conferences and workshops and also served as member of the international program committees for several international conferences. He was the Coordinator and PI of the international joint project entitled Digital Image and Video Forensics (acronym: DIVEFOR) funded through the Marie Curie Action under the EU's Seventh Framework Programme (FP7) from June 2010 to May 2014. He is currently the Coordinator and PI of the EU Horizon 2020 project, entitled Computer Vision Enabled Multimedia Forensics and People Identification (acronym: IDENTITY). The IDENTITY project has a consortium consisting of 16 institutions from 12 countries and will be running for four years, from January 2016 to December 2019.